Available online at www.sciencedirect.com
SCIENCE DIRECT®
International Journal of Heat and Mass Transfer 48 (2005) 4367–4383
International Journal of HEAT and MASS TRANSFER
www.elsevier.com/locate/ijhmt

Modeling of axially and transversely injected precursor droplets into a plasma environment ☆

Alper Ozturk, Baki M. Cetegen *

Department of Mechanical Engineering, University of Connecticut, 191 Auditorium Road, U-3139, Storrs, CT 06269-3139, USA

Received 11 March 2004; received in revised form 21 May 2005
Available online 19 July 2005

Abstract

Transport model of droplets injected axially or transversely into a plasma jet is presented. The droplets contain a ceramic precursor that precipitates in the vaporizing droplets. Droplet temperature and solute concentration distributions were predicted to estimate precipitation zones based on a homogeneous nucleation hypothesis. Effects of droplet size, injection velocity and injection angle were parametrically studied and the results were compared for axial and transverse injection. Axial injection is found to result in more rapid heat-up and precipitation than transverse injection. Computations suggest that small droplets form solid spherical particulates whereas larger droplets may form cenospheres and thin shell structures.
© 2005 Elsevier Ltd. All rights reserved.

Keywords: Droplet vaporization modeling; Plasma spraying; Ceramic coatings; Solution precursor plasma spray

1. Introduction

Ceramic coatings are used in high temperature applications to protect hardware against direct exposure to high temperatures and heat fluxes. For instance, yttria-stabilized zirconia coatings are typically applied as a top coat to protect components in applications such as gas turbines and combustors [1,2]. In other applications, alumina based coatings provide resistance to wear and prolong component service life [3]. The typical microstructure of thermal barrier coating contains 15–25% volume porosity to reduce the thermal conductivity of the coating [2]. Depending on the coating process, porosity can be in the form of interlamellar pores formed during rapid solidification of molten particles as in air plasma spray (APS) process [4]. Defects in the form of porosity and cracks contribute to both desirable and undesirable characteristics. While porosity and cracks lower the thermal conductivity, horizontal cracks can promote coating spallation.

Microstructure of the wear and corrosion resistant coatings is different from those of thermal barrier coatings. Defects present in the form of porosity and cracks are detrimental to the performance of wear and corrosion resistant coatings. Presence of these defects degrade the strength of the coating and allow diffusion of corrosive material into the coating and as such, eventually cause spallation and failure of the coating. In these applications, a ceramic coating is required to be dense so that the coating performance is acceptable. Several

☆ Revised text submitted to *Int. J. Heat Mass Transfer*.

* Corresponding author. Tel.: +1 860 486 2966; fax: +1 860 486 5088.
E-mail address: cetegen@engr.uconn.edu (B.M. Cetegen).

0017-9310/$ - see front matter © 2005 Elsevier Ltd. All rights reserved.
doi:10.1016/j.ijheatmasstransfer.2005.05.015

Nomenclature

B_M	Spalding mass transfer number, $B_M = (\chi_{v,\infty} - \chi_{v,s})/(1 - \chi_{v,s})$
B_T	Spalding heat transfer number, $B_T = (C_{P,v}(T_\infty - T_s))/(h_{fg} + Q_L/\dot{m})$
C_D	drag coefficient
C_P	specific heat
D_{12}	mass diffusivity of vapor phase into plasma gas
D_{za}	mass diffusivity of zirconium acetate into water
F	film thickness factor due to surface blowing, $F(B) = (1 + B)^{0.7}\ln(1 + B)/B$
h_{fg}	latent heat of vaporization for liquid
k	thermal conductivity
Le	Lewis number, $Le = D/\alpha$
$\dot{m}$	mass flow-rate at the droplet surface due to vaporization
Nu^*	Nusselt number corrected for the surface blowing effect, $Nu^* = 2 + (Nu - 2)/F(B_T)$
Nu	Nusselt number for a non-vaporizing sphere
Pe	Peclet number, $Pe = RePr$
Pr	Prandtl number, $Pr = \nu/\alpha$
Q_L	heat transfer rate into the liquid
r_s	instantaneous droplet radius
$\bar{r}_s$	non-dimensional instantaneous droplet radius, $\bar{r}_s = r_s/r_0$
Re	Reynolds number based on the droplet radius and the relative velocity between the droplet and the plasma
Sh^*	Sherwood number corrected for surface blowing effect, $Sh^* = 2 + (Sh - 2)/F(B_M)$
Sh	Sherwood number for a porous sphere
t	time
T	temperature
$\overline{T}$	non-dimensional temperature, $\overline{T} = (T - T_0)/T_0$
U	axial component of the droplet velocity
U_s	velocity of the circulating liquid at the droplet surface
U_∞	axial plasma velocity
V	radial component of the droplet velocity
V_r	radial component of the circulation velocity
$\overline{V}_r$	non-dimensional radial component of the circulation velocity, $\overline{V}_r = V_r/U_s$
V_θ	angular component of the circulation velocity
$\overline{V}_\theta$	non-dimensional angular component of the circulation velocity, $\overline{V}_\theta = V_\theta/U_s$

Greek symbols

α	thermal diffusivity
β	non-dimensional surface regression rate, $\beta = 0.5(d\bar{r}_s/d\tau)$
χ	mass fraction
$\bar{\chi}$	non-dimensional mass fraction, $\bar{\chi} = (\chi - \chi_0)/\chi_0$
η	non-dimensional radial coordinate, $\eta = r/r_s$
ν	kinematic viscosity
ρ	density
τ	non-dimensional time, $\tau = \alpha_L t/r_0^2$
θ	angular coordinate

Subscripts

g	gas phase
L	liquid phase
0	initial value
s	at the droplet surface
v	vapor phase
z	solute (zirconium acetate)
∞	plasma gas field at the far field

different coating deposition techniques, such as high velocity oxy-fuel (HVOF) combustion spraying [5] and D-gun™ spraying [6–8], have been used in producing such coatings.

The solution precursor plasma spray process involves a solution of ceramic precursor salts which is sprayed into a plasma gas environment (as opposed to powder in conventional APS), as schematically shown in Fig. 1. Thermal barrier coatings produced by the solution precursor plasma spray (SPPS) process have been shown to possess desirable microstructures composed of porosity in the form of an interconnected network of micrometer and nanometer sized voids generated due to the decomposition of the unpyrolyzed precursor and vertical cracks for strain tolerance under thermal cycling [9–11]. One of the main advantages of this process is the simplicity of the liquid precursor injection in the form of a spray as opposed to powder feeding with all its attendant problems. Other beneficial aspects of the process include ability to spray multi- layered or graded coatings. However, the porous microstructure favored in the thermal barrier coatings needs to be eliminated to generate dense coatings for other applications using the SPPS process. Porosity and vertical cracks appearing in the microstructure of the SPPS coatings are believed to be due to the tensile stresses that build up during the pyrolyzation of the precursor arriving at the surface in partially pyrolyzed or unpyrolyzed state [11].

In the SPPS process, the precursor is atomized into a spray by a pressure atomizer that generates droplets in

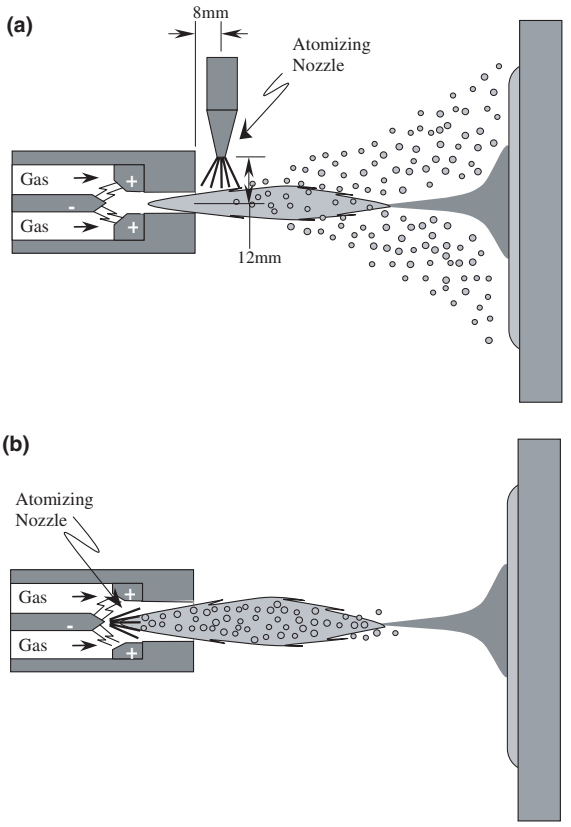

Fig. 1. Schematics of the solution precursor plasma spray process (a) for transverse injection and (b) for axial injection.

the range of 2–100 microns with velocities from 5 to 30 m/s resulting in a wide range of droplet momenta. These droplets are injected transversely into the plasma jet where they are entrained and heated. Some of the low momentum (small size, low velocity) droplets could not penetrate into the high velocity plasma jet and they are convected towards the substrate around the outer periphery of the plasma jet. They arrive on the substrate in a partially pyrolyzed form. These partially pyrolyzed droplets are further exposed to the hot plasma jet as the plasma torch scans the deposition surface. Decomposition of the partially processed droplets on the coating surface results in the micro and nanometer sized voids that constitute the porosity in the coating microstructure [12].

High velocity oxy-fuel (HVOF) spray process has been used in the production of dense ceramic coatings by spraying metallic or ceramic powders [5]. In this process, the powder is sprayed into the flame in an axial arrangement. Powder particles are accelerated towards the substrate with very high velocities (≈500 m/s) as compared to a plasma process (≈150 m/s) but the particle temperatures are significantly higher in the plasma process [13,14]. Dense coatings are formed in the HVOF process as a result of the high particle impact velocity. In the literature, axial injection of liquid precursor droplets has been implemented in a plasma spray to produce nano-sized ceramic powder and deposits [15]. The deposits of the yttria-stabilized zirconia were reported to be dense. The current understanding of the SPPS process suggests that if all of the liquid spray is introduced into the plasma, the pyrolysis on the substrate can be minimized or totally avoided resulting in a dense and potentially crack-free coatings.

Solution precursor plasma spray process has been extensively studied for the transverse injection of the precursor spray and a numerical model has been developed to analyze the heat and mass transfer in and around individual droplets [16]. The modeling approach utilized the measured, time-averaged velocity and temperature fields [14,17] into which the droplets were injected. The droplet vaporization and heat-up were computed along with the droplet trajectory. The predicted temperature and solute concentration profiles within those droplets were evaluated to estimate the formation zones of precipitates inside the droplets. In this study, vaporization and precipitate formation in droplets that are axially injected into the plasma jet are studied based on the numerical analysis of heat and mass transfer. Axial and transverse injection of the precursor droplets are compared to evaluate the differences for these two injection schemes. In the following, we first give a description of the model that was described in more detail earlier [16]. We then utilize the model results to highlight the differences between the axial and transverse injection schemes. The article is concluded by a summary of our findings.

2. Model description

Axial injection of precursor into the plasma jet is considered to be in the form of a spray that enters into the plasma core. As the droplets travel downstream in the plasma, they are accelerated towards the substrate by the plasma gases. From the point of entry into the plasma, droplets begin to heat up as they enter the hot plasma jet. During this process, the solvent starts to vaporize resulting in the increase of the solute concentration near the droplet surface. The precipitation of the solute ultimately results in the formation of ceramic precipitate. In the case of yttria-stabilized zirconia formation, the solution is composed of zirconium acetate and yttrium nitrate as solute and water as solvent.

The droplet motion in the plasma medium is calculated to determine the instantaneous location and size of the evaporating droplet. The plasma temperature and velocity fields were taken from the previous experiments [14,17]. Around each droplet, the vapor phase analysis includes the heat and mass transfer interactions

between droplet and the surrounding plasma field. In these computations, only single droplet injection was considered, thus neglecting the effects of neighboring droplets limiting the simulations to the dilute spray limit. The solute concentration distributions were then used to estimate the precipitation zones within each droplet by employing a simple, homogeneous nucleation hypothesis based on the critical supersaturation concentration of the solute.

Droplet motion in the plasma was calculated under the assumption that it is solely controlled by its aerodynamic drag. Neglecting the gravitational effects, the equations of droplet motion are written along with the droplet size variation as

$$\frac{\partial U}{\partial t} = \frac{3C_D}{8r_s}\frac{\rho_\infty}{\rho_L}|U_\infty - U|(U_\infty - U) \tag{1}$$

$$\frac{\partial V}{\partial t} = -\frac{3C_D}{8r_s}\frac{\rho_\infty}{\rho_L}V^2 \tag{2}$$

$$\frac{\partial r_s}{\partial t} = -\frac{\dot{m}}{4\pi\rho_L r_s^2} \tag{3}$$

Variables used in these equations are defined in the nomenclature. The thermophysical properties of the plasma medium were determined from the property database given in the literature [18] based on the plasma gas composition (80% mole Ar, 20% mole H_2) and the measured plasma temperature field. The drag coefficient, C_D, is modified for the surface blowing effects as suggested by Yuen et al. [19] as

$$C_D = \frac{24}{Re(1+B_M)} \tag{4}$$

Above set of equations require the mass vaporization rate, $\dot{m}$, which is obtained from the vapor and liquid phase analyses. The flow relaxation times for the liquid phase is much longer than the vapor phase, therefore, the vapor phase solution can be approximated as quasi-steady state. The mass vaporization rate can be calculated from both the Nusselt number for heat transfer and the Sherwood number for mass transfer as

$$\dot{m} = 2\pi\rho_g D_{12} r_s Sh^* \ln(1+B_M) \tag{5}$$

$$\dot{m} = 2\pi\frac{k_g}{C_{P,v}} r_s Nu^* \ln(1+B_T) \tag{6}$$

In these equations, Nusselt number, Nu^*, and Sherwood number, Sh^*, are based on the non-vaporizing sphere, modified for the vaporization effects because of the varying film thickness around the droplet. The mass vaporization rate, $\dot{m}$ defined in Eqs. (5) and (6) cannot be calculated since the Spalding heat and mass transfer numbers, B_T and B_M, includes droplet surface temperature and vapor concentration, which are determined as a part of the coupled solution. These equations are supplemented with the Clapeyron equation and Raoult's Law to determine the mass vaporization rate, surface temperature and surface vapor concentration.

The surface temperature and mass vaporization rate are then used as boundary conditions in the solution of the conservation of energy and species equations in the liquid phase. The droplet sizes are small (1–40 μm) such that the surface tension forces maintain the droplets in spherical shape. As the droplets travel towards the substrate, the shear around the droplet due to the relative velocity between the droplet and the surrounding gas flow generates an axisymmetric recirculation within the droplet. Although this droplet internal flow field can be determined by the solution of the Navier–Stokes equations, an approximation of this field to the well known Hill's spherical vortex has been shown to be adequate [20]. Non-dimensionalized conservation of energy equation and the associated initial and boundary conditions can be written in the axisymmetric spherical coordinates as [16]

$$\begin{aligned}\bar{r}_s^2\frac{\partial\overline{T}}{\partial\tau} + (0.5Pe_L\overline{V}_r\bar{r}_s - \beta\eta)\frac{\partial\overline{T}}{\partial\eta} + 0.5Pe_L\frac{\overline{V}_\theta\bar{r}_s}{\eta}\frac{\partial\overline{T}}{\partial\theta}\\ = \frac{1}{\eta^2}\frac{\partial}{\partial\eta}\left(\eta^2\frac{\partial\overline{T}}{\partial\eta}\right) + \frac{1}{\eta^2\sin\theta}\frac{\partial}{\partial\theta}\left(\sin\theta\frac{\partial\overline{T}}{\partial\theta}\right)\end{aligned} \tag{7}$$

$$\begin{aligned}&\tau = 0 \rightarrow \overline{T} = 0\\ &\eta = 1 \rightarrow \begin{cases}\dfrac{\partial\overline{T}}{\partial\theta} = 0\\ \displaystyle\int_0^\pi \frac{\partial\overline{T}}{\partial\eta}\sin\theta\,d\theta = Q_L/(2\pi r_s k_L T_0)\end{cases}\\ &\theta = 0,\ \ \pi \rightarrow \frac{\partial\overline{T}}{\partial\theta} = 0\end{aligned} \tag{8}$$

In a similar manner, the conservation of species equation and its initial and boundary conditions can be written as [16]

$$\begin{aligned}Le_L\bar{r}_s^2\frac{\partial\bar{\chi}_z}{\partial\tau} + (0.5Pe_L Le_L\overline{V}_r\bar{r}_s - Le_L\beta\eta)\frac{\partial\bar{\chi}_z}{\partial\eta}\\ + 0.5Pe_L Le_L\frac{\overline{V}_\theta\bar{r}_s}{\eta}\frac{\partial\bar{\chi}_z}{\partial\theta}\\ = \frac{1}{\eta^2}\frac{\partial}{\partial\eta}\left(\eta^2\frac{\partial\bar{\chi}_z}{\partial\eta}\right) + \frac{1}{\eta^2\sin\theta}\frac{\partial}{\partial\theta}\left(\sin\theta\frac{\partial\bar{\chi}_z}{\partial\theta}\right)\end{aligned} \tag{9}$$

$$\begin{aligned}&\tau = 0 \rightarrow \bar{\chi}_z = 0\\ &\eta = 1 \rightarrow \begin{cases}\dfrac{\partial\bar{\chi}_z}{\partial\theta} = 0\\ \displaystyle\int_0^\pi \frac{\partial\bar{\chi}_z}{\partial\eta}\sin\theta\,d\theta = \dot{m}/(2\pi r_s\rho_L D_{za}\chi_{z,0})\end{cases}\\ &\theta = 0,\ \ \pi \rightarrow \frac{\partial\bar{\chi}_z}{\partial\theta} = 0\end{aligned} \tag{10}$$

Given the initial droplet size and injection velocity, solution of these equations along the droplet trajectory are sought. The details of the solution methodology have been presented previously [16]. Briefly, the system of

equations is numerically solved using the DuFort–Frankel method by second order discretization in time and space. The convergence and consistency of the numerical routine is ensured by properly selecting the time and space intervals. The model results were compared with the experimental results of Daif et al. [21] for a binary fuel droplet whose composition was 75% decane and 25% heptane as presented in [16]. The maximum deviations in the droplet size and temperature between the model results and the experiments were found to be 6% and 5%, respectively.

3. Results and discussion

Computations were performed for different initial size droplets and injection velocities for the axial injection scheme. The analysis also included effects of slightly angled axial injection of the droplets. In this analysis, initial droplet sizes were taken as 10, 20, 30 and 40 μm with the nominal injection velocity of 12 m/s. The droplet injection velocity variation was studied by considering 0, 12, 24 and 36 m/s for a 20 μm droplet to reflect the distribution of different velocities obtained from the precursor atomizer used in the SPPS process. For the atomizer used in the transverse injection experiments, the half cone angle of the spray was measured to be approximately 10°, therefore droplet injection angle variations were performed by considering the injection angles of 0°, 5°, and 10° for the baseline case of 20 μm droplet injected with 12 m/s velocity. The results of the axially injected droplets were compared with those for the transverse injection by performing computations for the transverse injection for the two conditions of 20 and 40 μm droplets injected at 12 m/s velocity.

The plasma velocity and temperature field used in this study are shown in Fig. 2. The velocity field was measured by laser Doppler velocimetry and the temperature field was determined by emission spectroscopy of argon [17]. Thermophysical properties of the plasma gases and the precursor solution were obtained from the data in the literature. The thermophysical property database for the plasma gases was obtained from reference [18] which contains property tables as a function of plasma gas composition and temperature. The data were fit into temperature dependent expressions as listed in Table 1 for the plasma gas mixture of 80% mole Ar and 20% mole H_2. The density, thermal conductivity and specific heat of solvent (water) were obtained from the temperature dependent data as listed in Table 2. Even though the binary diffusivity and saturation mass fraction of the solute (zirconium acetate) are temperature dependent, they were taken as 10^{-9} m^2/s and 0.562, respectively based on the only available data in the literature [22,23].

3.1. Droplet size effects

The droplet size effects were studied by considering 10, 20, 30 and 40 μm initial size droplets injected into the plasma field axially. For comparison, 20 and 40 μm droplets were also injected transversely at

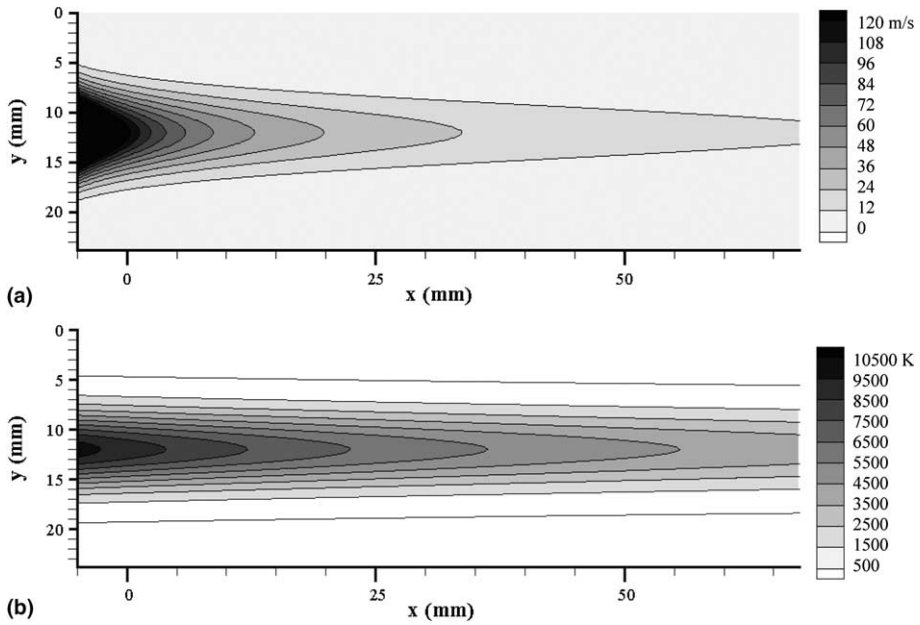

Fig. 2. Axial plasma velocity (a) and temperature (b) fields used in this study.

Table 1
Thermophysical properties of the plasma gas

Plasma properties [18]	
Density (kg m^{-3})	$\rho = a(T+b)^c$ $a = 1.397\times10^{3}$ $b = 1.376\times10^{2}$ $c = -1.160$
Dynamic viscosity (kg m^{-1} s^{-1})	$\mu = a + bT + cT^2$ $a = 2.130\times10^{-5}$ $b = 3.454\times10^{-8}$ $c = -9.669\times10^{-13}$
Specific heat (J kg^{-1} K^{-1})	$C_P = a + bT$ $a = 9.376\times10^{2}$ $b = 1.974\times10^{-1}$
Thermal conductivity (W m^{-1} K^{-1})	$k = a + bT$ $a = 1.125\times10^{-2}$ $b = 5.499\times10^{-5}$

Tabulated data available in the property database [18] is curve-fitted in the temperature range of 500–7000 K.

Table 2
Thermophysical properties of the liquid and vapor phases

Liquid and vapor properties	
Mass diffusivity of zirconium acetate into water [22] (m^2 s^{-1})	$D_{za} = 1.0\times10^{-9}$
Saturation concentration of zirconium acetate in water [23] (kg, ZA-kg, mix^{-1})	$\chi_{sat} = 0.562$
Mass diffusivity of vapor into ambient [25] (m^2 s^{-1})	$D_{12} = 2.6\times10^{-5}$
Density [25] (kg m^{-3})	$\rho_L = a + bT + cT^2$ $a = 1.119\times10^{3}$ $b = 1.705$ $c = -3.517\times10^{-3}$ $\rho_s = a\exp(b/T)$ $a = 2.248\times10^{5}$ $b = -4.869\times10^{3}$
Thermal conductivity [26] (W m^{-1} K^{-1})	$k_L = a + bT + cT^2$ $a = -3.509\times10^{-1}$ $b = 5.017\times10^{-3}$ $c = -6.059\times10^{-6}$
Dynamic viscosity [26] (kg m^{-1} s^{-1})	$\mu_L = a\exp(b/T)T^c$ $a = 4.217\times10^{-30}$ $b = 4.425\times10^{3}$ $c = 8.035\times10^{0}$
Enthalpy of vaporization [27] (J kg^{-1})	$h_{fg} = a + bT + cT^2$ $a = 2.350\times10^{6}$ $b = 2.348\times10^{3}$ $c = -6.875\times10^{0}$
Specific heat [27] (J kg^{-1} K^{-1})	$C_{P,L} = a + bT + cT^2$ $a = 7.453\times10^{3}$ $b = -1.915\times10^{1}$ $c = 2.747\times10^{-2}$ $C_{P,s} = a + bT + cT^2$ $a = 6.626\times10^{3}$ $b = -2.909\times10^{1}$ $c = 6.618\times10^{-2}$

Liquid and vapor properties are taken from various sources as indicated. Liquid properties are curve-fitted in the temperature range of 273–400 K, whereas, vapor properties are curve-fitted in the temperature range of 273–700 K.

12 mm offset from the plasma jet centerline in the radial direction as schematically shown in Fig. 1a. All of the droplets were injected with a nominal initial velocity of 12 m/s. A comparison of the plasma temperatures and velocities experienced by these droplets along their trajectories is shown in Fig. 3. For the axially injected droplets, the plasma temperatures along the droplet trajectory decrease from initially very high temperatures (≈9000 K) as the droplets travel along the plasma axis, whereas the plasma temperature increases as the transversely injected droplets begin to penetrate into the plasma. The plasma temperature to which droplets are exposed influences the droplet heat-up and vaporization. Similarly, the plasma gas velocities experienced by the axially injected droplets are very high in the plasma core and droplets travel to lower velocity regions further downstream. The plasma temperatures and velocities experienced by the two transversely injected droplets are significantly different. The 40 μm droplet that reduces in size (Fig. 4a) during the flight experiences higher plasma temperatures and velocities as a result of its high initial momentum allowing it to penetrate deeper into the plasma. In this and subsequent figures, the computational results terminate at different convection times for different size droplets. This is because the computation is stopped when the droplet surface solute mass fraction reaches unity by which time the precipitation should have commenced. The time at which this condition is reached is different for different size droplets since they traverse different regions of the plasma and the internal transport characteristics are different for different sizes.

Variation of instantaneous droplet sizes and droplet surface temperatures are shown in Fig. 4. The droplet size reduction for smaller droplets is high since the droplet surface temperature for the axially injected droplets increases faster for smaller droplets. This is due to the lower levels of internal circulation within the smaller droplets resulting in less effective mixing within the droplet and consequently higher droplet surface vaporization. In the case of larger droplets, more efficient internal circulation within the droplet carries away the high temperature liquid near the droplet surface and has a suppression effect on the rate of vaporization. It is noteworthy that the droplets reach the solute saturation earlier for the axial injection than

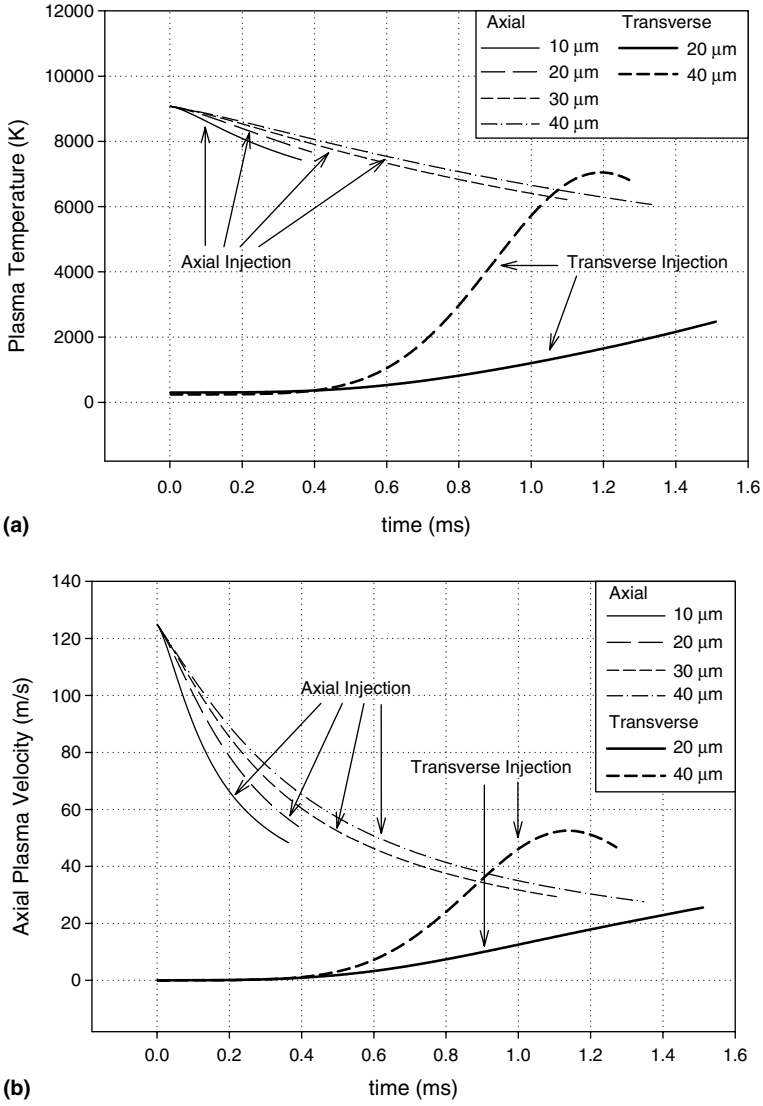

Fig. 3. Comparison of (a) plasma temperature, and, (b) plasma velocity fields experienced by 10, 20, 30 and 40 μm droplets injected axially and 20 μm droplet injected transversely as they are convected downstream towards the substrate.

the transversely injected droplets as indicated by the termination times of the calculation in Fig. 4a. This is due to the lower plasma temperatures that the droplets are exposed to and the slower vaporization rates in the transverse injection case. Although the transversely injected 40 μm droplet reaches higher temperatures in the core of the plasma, the large droplet mass and higher degree of internal circulation result in slower vaporization rates. The calculations are stopped when the surface concentration of the droplet reaches unity (pure solute) after which no vaporization is expected since pure solute prohibits the diffusion of the solvent (water) onto the droplet surface. It is also expected that precipitation would have commenced by that time. In the transverse injection case, the transport of solute from high concentration (surface) to low concentration (droplet interior) regions allow the solvent to diffuse towards the outer surface more efficiently and thus the surface concentration reaches unity at later times.

The droplet surface temperatures are shown in Fig. 4b. The surface temperatures of the axially injected droplets increase rapidly to values around 370 K, whereas the surface temperatures of the transversely injected droplets show an initial depression and then gradually increase at later times. The axially injected droplets experience a high temperature difference and large relative velocity at the initial stages of injection which

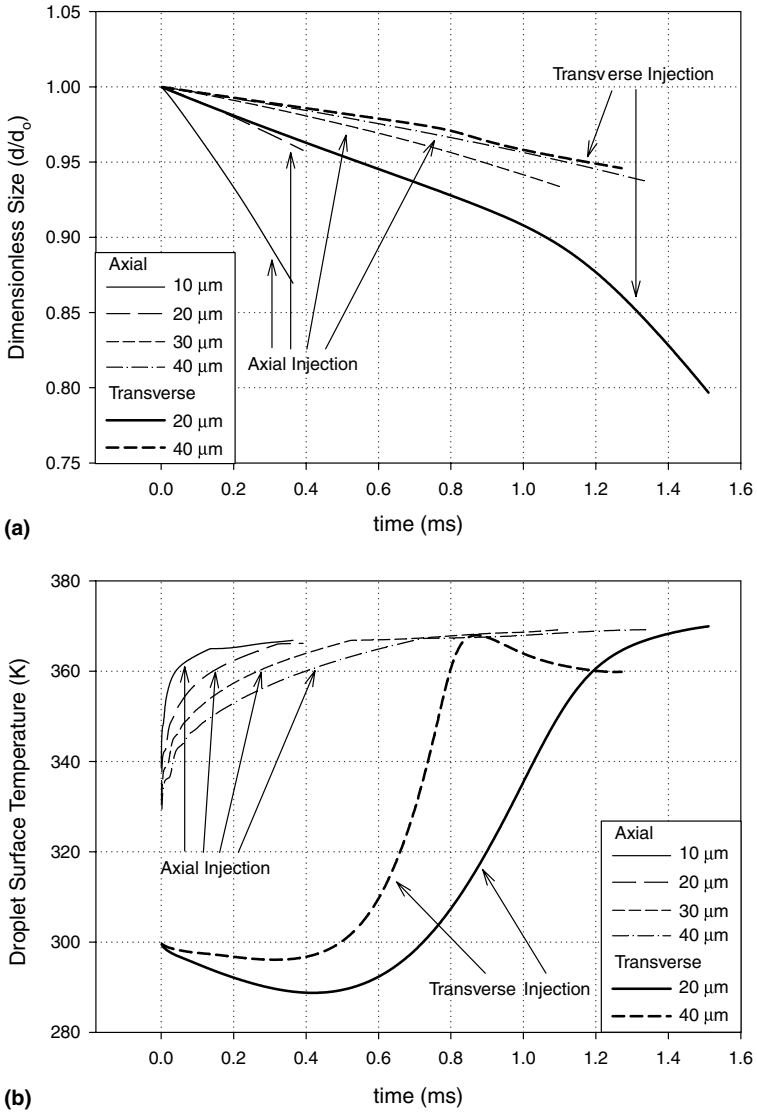

Fig. 4. Comparison of (a) droplet size reduction and (b) droplet surface temperature of 10, 20, 30 and 40 μm droplets injected axially and 20 μm droplet injected transversely as they are convected downstream towards the substrate.

enhances the heat transfer from the high temperature plasma to the droplet. On the other hand, the transversely injected droplets first experience ambient temperature conditions which lead to evaporative sub-cooling and the depression in the droplet surface temperature. As the droplets penetrate into the high temperature regions of the plasma, the droplet surface temperature increases; eventually approaching those for the axially injected droplets. The 40 μm droplet experiences a second depression in its surface temperature at later times. This is because of the enhanced mixing effect within the droplet due to the higher relative velocity as the droplet penetrates into the plasma jet.

3.2. Injection velocity effects

Injection velocity is also considered to be one of the important factors affecting the droplet heat up and vaporization. In order to analyze the effects of injection velocity, four cases of axial injection were compared with the transverse injection at nominal conditions. In this study, droplet injection velocities of 0, 12, 24 and 36 m/s were considered for the axial injection along with 12 m/s for the transverse injection. The initial droplet size was 20 μm in all cases. In Fig. 5, the plasma temperatures and velocities experienced by the droplets are shown. Plasma temperatures for the axially injected droplets show

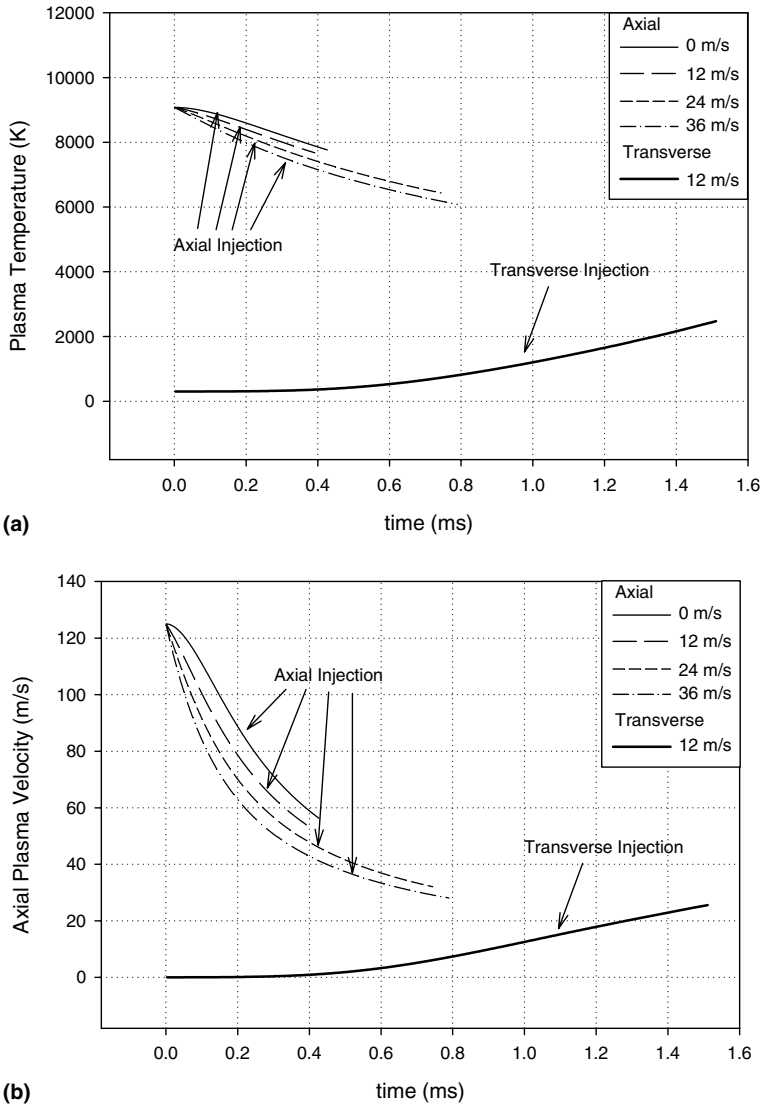

Fig. 5. Comparison of (a) plasma temperature, and, (b) plasma velocity fields experienced by droplets injected axially with 0, 12, 24 and 36 m/s velocity and droplet injected transversely with 12 m/s velocity as they are convected downstream towards the substrate.

a faster decay for the droplets that are injected at higher velocities as depicted in Fig. 5a. This is expected since residence time in the high temperature core of the plasma for droplets with higher initial velocities would be shorter, and these droplets would travel faster towards the cooler downstream regions (see plasma temperature distribution in Fig. 2b). The droplets injected at 36 m/s reside in a region where the plasma temperature is about 6000 K when the surface concentration reaches unity (pure solute). In contrast, the transversely injected droplet experiences lower peak temperatures of the order of 2500 K since it does not penetrate into the high velocity plasma core due to its relatively low momentum. Similarly, plasma velocities along the droplet trajectory, shown in Fig. 5b, indicate that the axially injected droplets experience much higher velocities compared to the transversely injected droplets as expected. Droplets with high injection velocities travel faster through the plasma and experience faster decay of the local plasma velocity. On the other hand, the transversely injected droplet experiences stagnant ambient environment initially, and then as it penetrates into the jet, plasma velocities start to increase as shown in Fig. 5b.

The droplet size reduction and droplet surface temperatures are shown in Fig. 6. It is seen that low injection velocities result in faster vaporization rates and this is because of the high initial relative velocity between the droplet and the plasma. On the other hand, as the droplets are injected at higher velocities, the

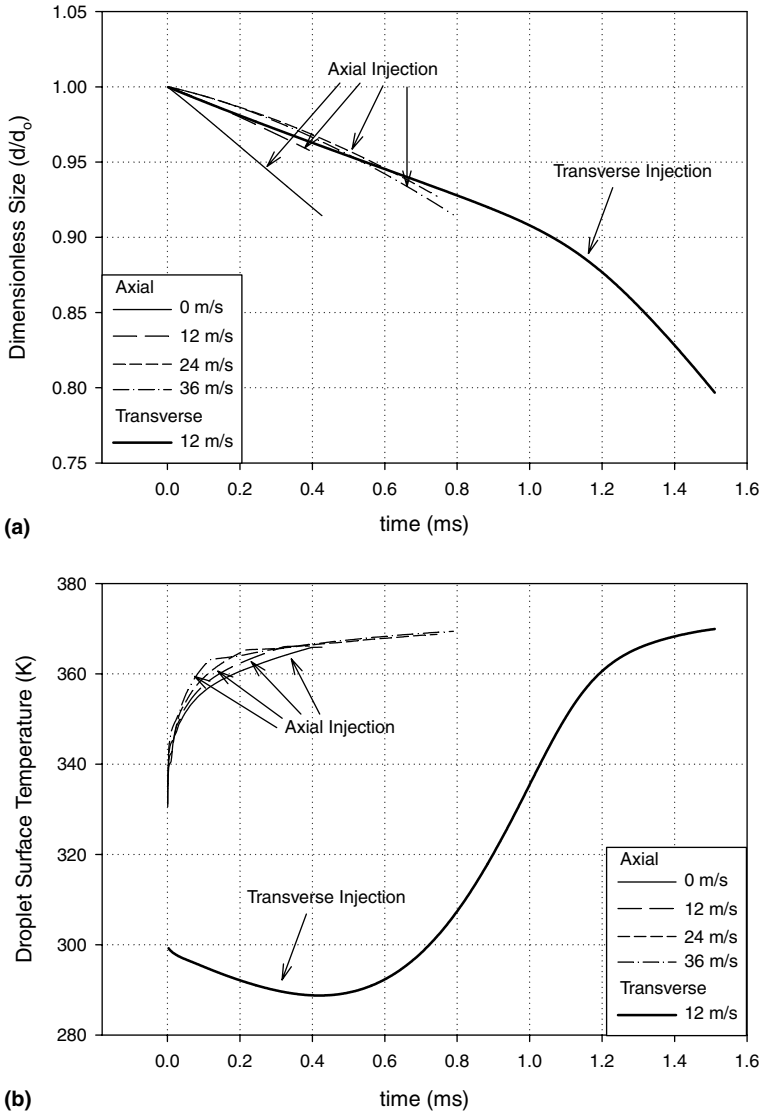

Fig. 6. Comparison of (a) droplet size reduction and (b) droplet surface temperature of droplets injected with 0, 12, 24 and 36 m/s velocities axially and 12 m/s velocity transversely as they are convected downstream towards the substrate.

plasma velocity and the droplet velocity become comparable, thus the relative velocity decreases resulting in a similar droplet size variations and vaporization rates for 24 and 36 m/s injection velocities. The similarity of the droplet size reduction for the axially injected droplets at 12, 24 and 36 m/s can be explained as follows. The increasing droplet injection velocity translates to a reduction in the initial relative velocity between the droplet and the plasma resulting in weaker internal circulation. Due to this weak circulation, droplet surface temperatures reach higher values as shown in Fig. 6b. While this would result in higher rate of vaporization, the solute build-up near the droplet surface inhibits the transport of solvent to the droplet surface by diffusion in these cases of weaker internal circulation. Hence, the two effects combine to yield similar droplet size reduction rates as shown in Fig. 6a. Transverse injection shows an initial droplet surface temperature depression when the droplet is traveling in the outer edge of the plasma followed by a steep increase as it penetrates into high temperature region. The time for the surface solute concentration to reach unity is significantly longer in this case.

3.3. Injection angle effects

Droplets generated by air-blast atomizers are typically confined to a conical region. In the solution-precur-

sor plasma spray process where the droplets are injected transversely as a spray, the spray cone or initial droplet injection angle has been shown to influence the droplet temperatures and trajectories [16]. In the axial injection case, injection angle is still an important factor as the droplet may be launched into the plasma within a narrow angle with respect to the plasma axis. Thus, the effect of the injection angle was studied for a total spray cone angle of 20°. The simulations were performed for axially injected droplets at 0°, 5° and 10° from the plasma jet axis to cover the spray cone angle as well as for a transversely injected droplet at the same nominal conditions. Trajectories of these droplets in the plasma jet are shown in Fig. 7. It is found that the axially injected droplets follow almost straight line trajectories whereas the transversely injected droplet is deflected by the plasma jet and enters into the jet gradually.

The plasma temperatures experienced by the axially injected droplets are quite similar for the early stages of droplet trajectory as depicted in Fig. 8a. At the latter stages, however, the temperature differences can amount to about 1000 K due to the differences in the droplet trajectories. Similarly, it is seen in Fig. 8b that the plasma velocities for droplets injected at initially different angles are similar, but they differ considerably from that for the transversely injected droplets. At residence times greater than 1.3 ms, axially injected droplets reach plasma regions where the velocities are lower than those for the transversely injected droplets. These results indicate that the vaporization rate and droplet surface temperature would not be significantly affected due to the variation in the injection angle for axial injection. The droplet size variations shown in Fig. 9a, indicate that the injection angles of 0°, 5° and 10° result in almost identical rates of droplet size reduction in the early stages, due to similar plasma jet conditions. Later on, the variations in the droplet sizes begin to emerge. The transverse injection has slower vaporization rates and diameter variation due to lower temperatures experienced by these droplets. Also, the axially injected droplets have similar surface temperatures throughout their residence in the plasma jet, whereas, the transversely injected droplets experience low temperatures in the early stages, and then these temperatures gradually increase as they penetrate into the plasma as depicted in Fig. 9b.

3.4. Temperature and solute concentration distributions

Determination of temperature and solute concentration distributions within a droplet was one of the main objectives of this study. With these distributions, one can estimate the precipitation zones around the droplets by employing a simple homogeneous nucleation hypothesis. The precipitation of zirconium acetate within the droplets is a process which is a function of both local temperature and solute concentration under equilibrium conditions. It could however involve kinetic effects under conditions of rapid concentration and temperature variation. Typically, the solution is supersaturated locally due to vaporization of the solvent and upon reaching a critical supersaturation level, the precipitation would be initiated resulting in the precipitation of acetate groups within the droplet at locations where the saturation concentration is exceeded as suggested

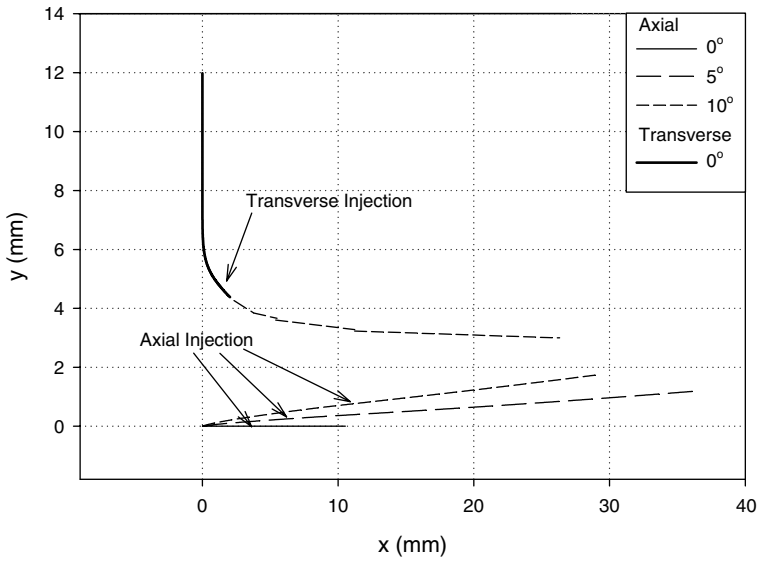

Fig. 7. Trajectories of droplets injected axially with 0°, 5° and 10° injection angle and droplet injected transversely as they are convected downstream towards the substrate.

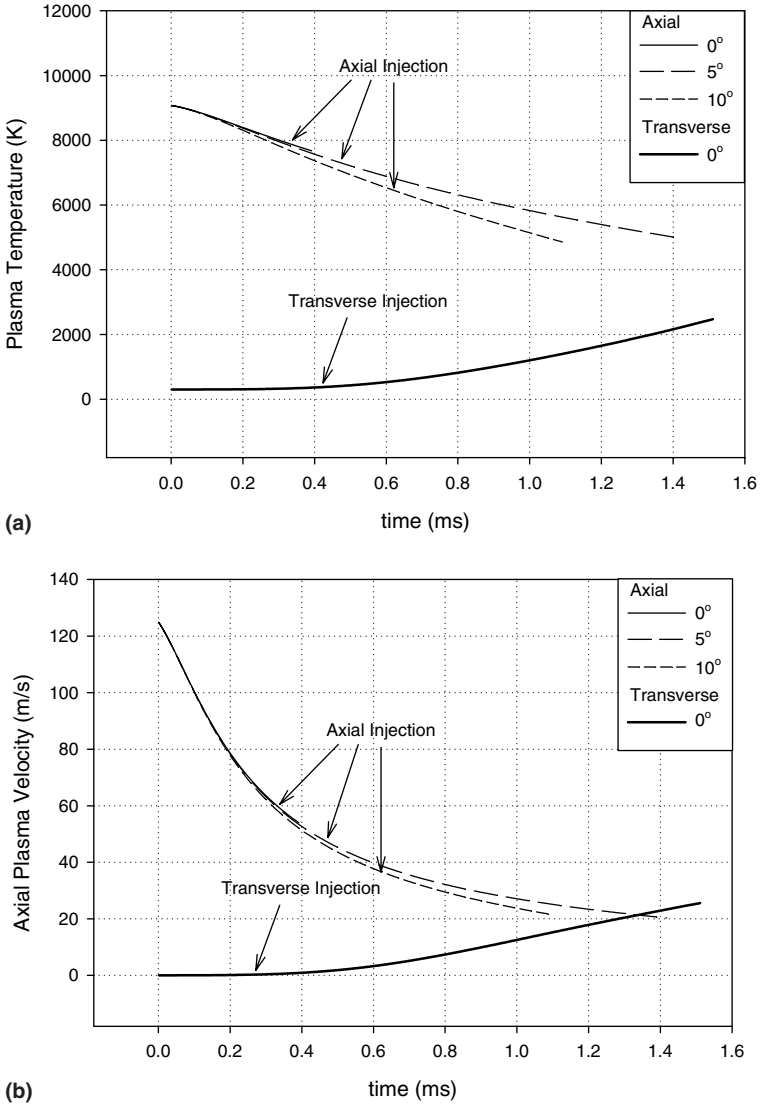

Fig. 8. Comparison of (a) plasma temperature, and, (b) plasma velocity fields experienced by droplets injected axially with 0°, 5°, and 10° injection angle and droplet injected transversely as they are convected downstream towards the substrate.

in the literature [22]. Heterogeneous nucleation, which consists of multiple nucleation sites within the droplet, is expected to result in more complex precipitation patterns. However, only homogeneous nucleation is considered in this study, due to the complexities associated with heterogeneous nucleation and the lack of adequate models for implementation.

The solute concentration and temperature distributions within a droplet need to be known to determine the initiation of precipitation. However, there are currently no available data on the temperature dependent saturation concentration in the literature for the material system in this application. Given this, the value of the saturation concentration was taken as constant, $\chi_z = 0.562$, as suggested by Zhang and Messing [23]. The highest concentrations within the droplet are expected to occur near the droplet surface since solvent loss occurs there. As the high levels of supersaturation is observed at the surface, the precipitation is expected to begin in these regions and subsequently catalyze the precipitation in the supersaturated regions. In this study, the temperature and concentration histories of the droplets were determined for droplets of different sizes. This information was used to estimate the precipitation zones within droplets suggesting the possible morphologies of the particulates.

The baseline case for the axially injected droplets was taken to be 20 μm droplet injected at a velocity of 12 m/s

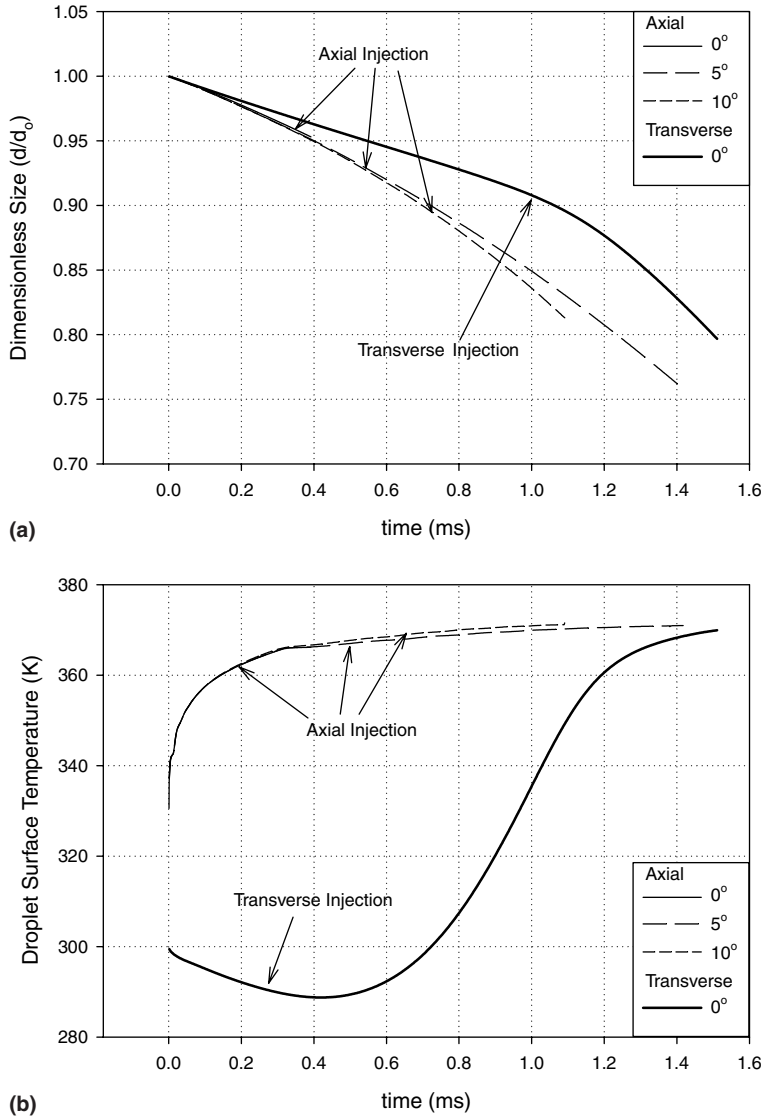

Fig. 9. Comparison of (a) droplet size reduction and (b) droplet surface temperature of droplets injected axially with 0°, 5° and 10° injection angle and droplet injected transversely as they are convected downstream towards the substrate.

along the plasma jet axis. The temperatures and concentration distributions within the droplet at two instants in time are shown in Fig. 10. These two time instants were chosen as the time when droplet surface reaches to pure solute state (0.4 ms) and half of that time (0.2 ms). It is seen that in the early stages of the droplet lifetime, the diffusion and advection processes are comparable and temperature gradients are slightly higher near the forward stagnation point as a result of circulation within the droplet. At longer times, the relative velocity between the droplet and the plasma gases diminish (and hence the circulation within the droplet weakens) and the heat transfer mode becomes almost purely conduction as evident by the concentric shapes of the isotherms. One should note that, the temperature variation within the droplets is very small and droplets are essentially isothermal. On the other hand, the mass transfer Peclet number is very high due to the low diffusivity of zirconium acetate in water and consequently the concentration distributions exhibit a highly convective behavior where the iso-concentration lines almost coincide with the flow streamlines within the droplet. In contrast to the axially injected droplet, transverse injection at similar times after injection has different characteristics as depicted in Fig. 10. Overall, the droplet temperatures for transverse injection are lower than those for axial injection. The temperature distributions exhibit mostly diffusive nature with some convection effects. Early on,

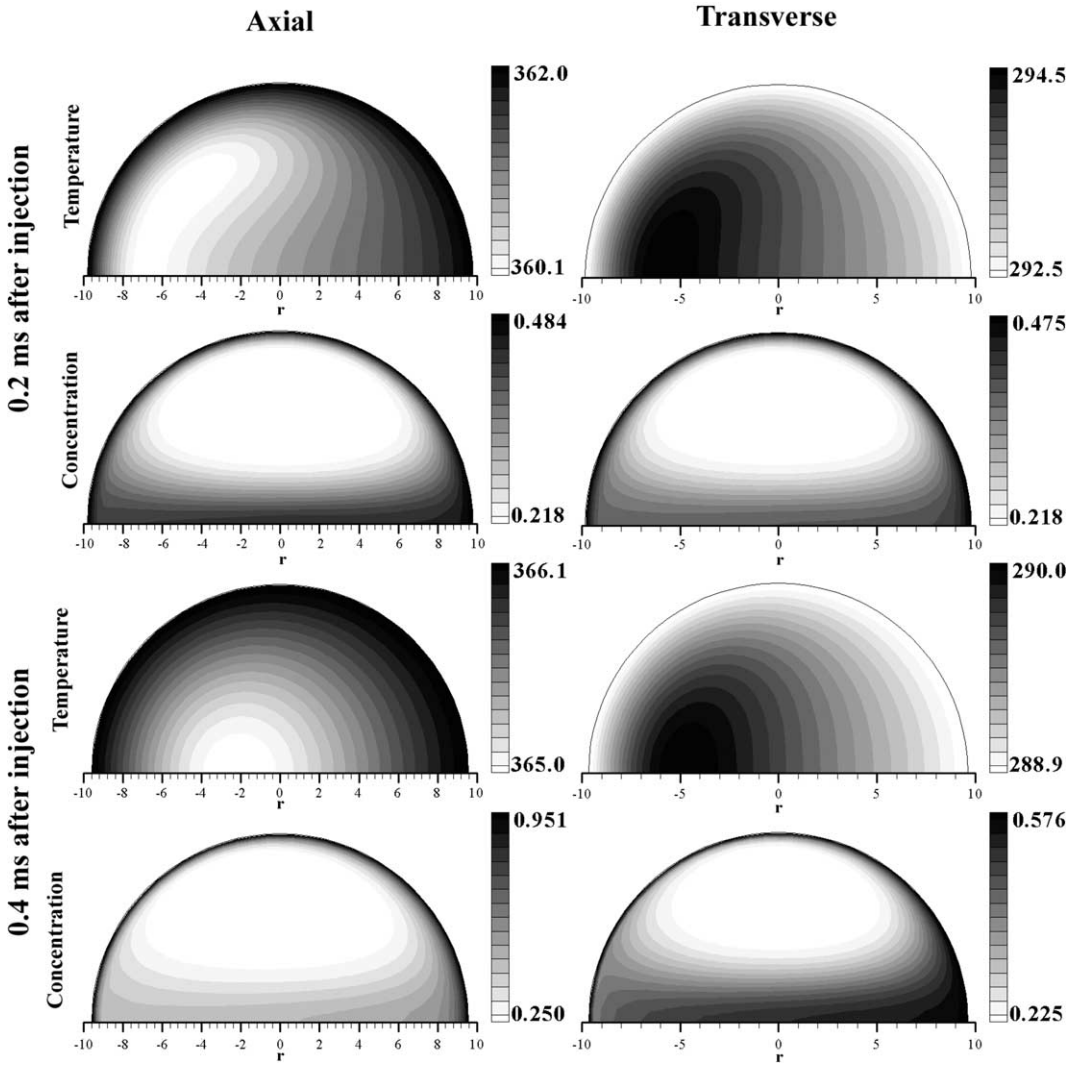

Fig. 10. Temperature and concentration distributions within an axially injected 20 μm droplet and a transversely injected droplet 0.2 ms and 0.4 ms after injection.

the surface temperature of the transversely injected droplet is lower than the droplet interior indicating that the droplet is in the evaporative cooling phase and the droplet has not yet penetrated into the plasma. Concentration distributions show that the surface solute concentrations build up primarily as a result of low circulation and slow diffusion creating a thin layer of high concentration zone near the surface of the droplet. The surface solute concentrations at 0.4 ms after injection are significantly higher for the axially injected droplet as compared to those for transverse injection.

Size variations in the axially injected droplets were also studied and are shown in Fig. 11. The temperature and concentration distributions are shown for 10 μm and 30 μm droplets. For 10 μm droplet, it is seen that the temperature distributions show low Peclet number characteristics, and the dominant heat transfer mode throughout droplet's lifetime is conduction as evident by the concentric shapes of the isotherms. Uniformly high temperatures are observed within the droplet and temperatures reach high values rapidly and an equilibrium is sustained between the rate of heat transfer to the droplet and the rate of vaporization from the surface. The concentration distributions show the high concentration regions penetrating into the core of the droplet and showing large areas at high concentration levels at 0.36 ms after injection. In comparison, larger 30 μm droplet exhibits temperature distributions dominated by convective effects in the early stages which diminish as the relative velocity between the droplet

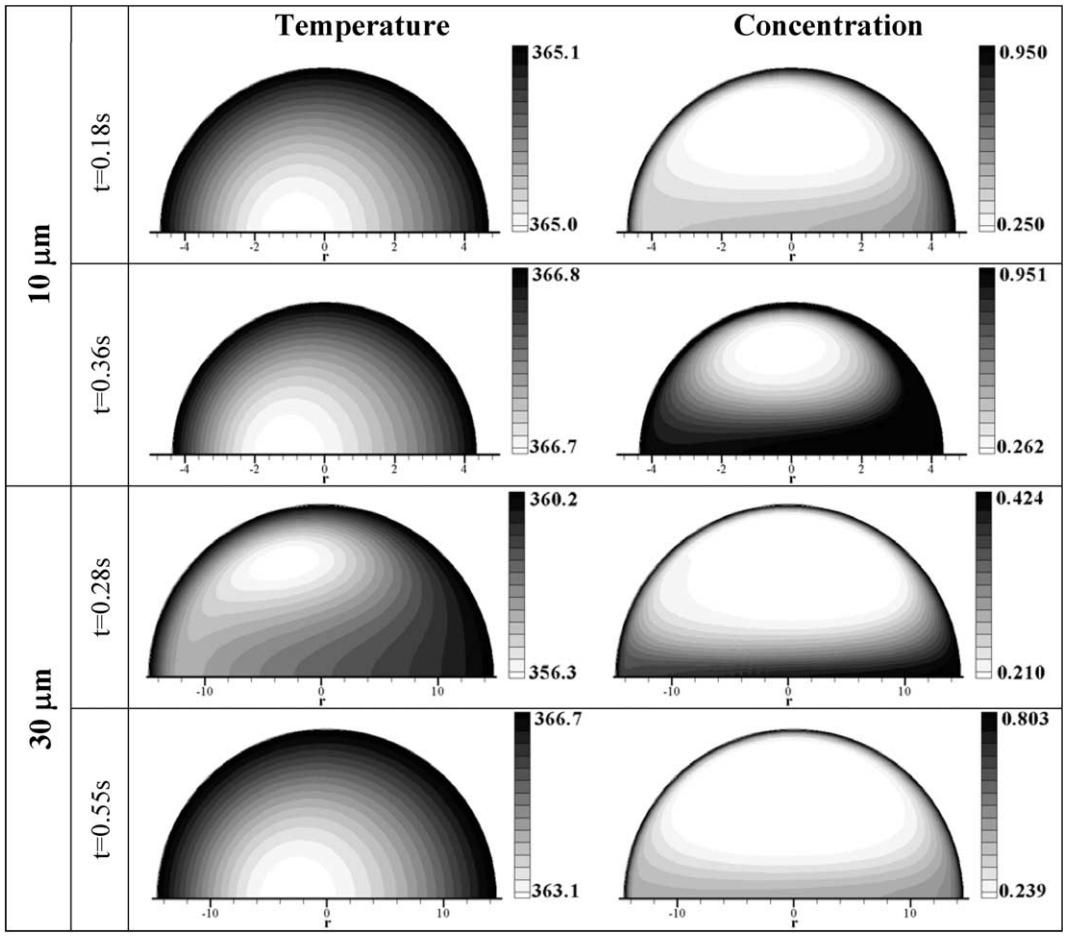

Fig. 11. Temperature and concentration distributions within an axially injected 10 μm droplet 0.18 ms and 0.36 ms after injection and an axially injected 30 μm droplet 0.28 ms and 0.55 ms after injection.

and plasma jet approaches zero in the latter stages of droplet lifetime.

3.5. Precipitation zones within the droplets

One of the main objectives of this study was to estimate the precipitation zones within the droplets such that the possible precipitate morphologies can be evaluated. Based on the simple homogeneous nucleation hypothesis employed in this study, the estimates of precipitation zones within the droplets were made for different droplet sizes as depicted in Fig. 12. First, the comparison of the axial and transverse injection is shown in Fig. 12a and b. It is seen that 0.4 ms after injection, the axially injected droplet generates a shell structure around the droplet, whereas, the transversely injected droplet has no solute concentration saturation regions for the onset of precipitation. This droplet is still in the heat-up phase and it is in liquid phase. The thin shell formed in the axially injected droplet prohibits diffusion of solvent onto the droplet surface trapping the liquid within a shell. Upon further heating as the droplet travels, several different scenarios are possible. In one of these, the internal liquid might start boiling and due to the build up of the internal pressure, the droplet might burst exposing the internal liquid to further atomization or fragmentation as well as producing a fractured thin shell of precipitates. Another probable scenario includes gelation and similar formation paths. However, present model cannot incorporate these possible scenarios due to complex nature of these phenomena and the lack of adequate models for these processes. Smaller droplets result in formation of interesting structures as shown in Fig. 12c and d. Simulation of a 5 μm droplet shows a very large precipitation zone, and suggests that the droplet is almost fully precipitated. On the other hand, when the surface concentration reaches pure solute, the internal structure of a 10 μm droplet consists of a ceno-sphere interconnected along the axis of the droplet.

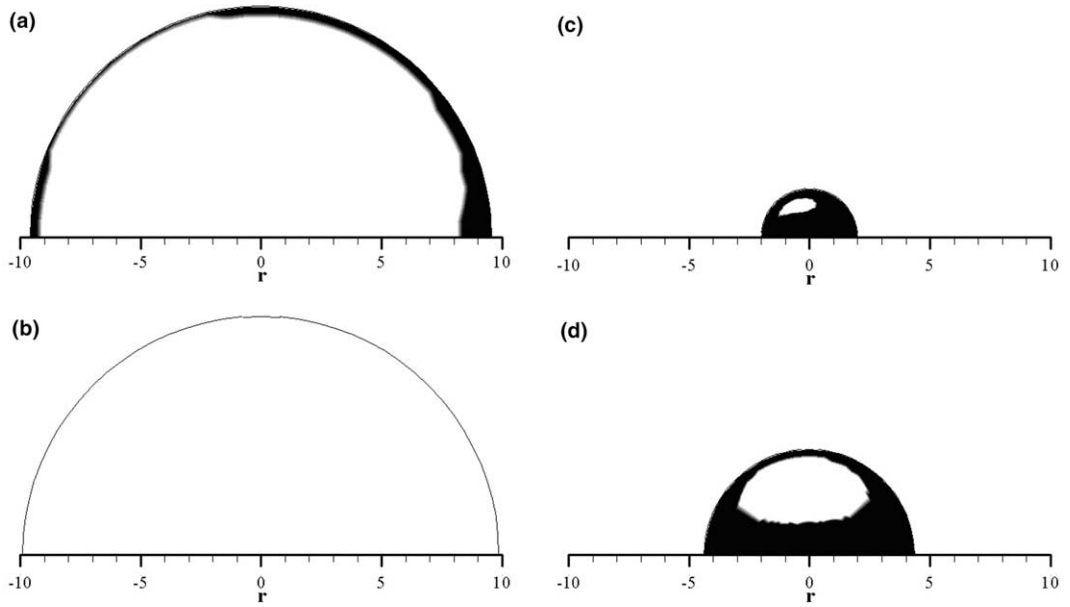

Fig. 12. Precipitation zones within the droplets for (a) axially injected 20 μm droplet 0.4 ms after injection, (b) transversely injected 20 μm droplet 0.4 ms after injection, (c) axially injected 5 μm droplet 0.2 ms after injection, and, (d) axially injected 10 μm droplet 0.36 ms after injection.

4. Conclusions

The solution-precursor plasma-spray process can produce ceramic coatings with nanometer size features. In the earlier studies, it has been shown that thermal barrier coatings can be produced with superior properties, and due to the generic nature of the process, it can be expanded into other ceramic microstructures. Dense ceramic coatings can be obtained by axial injection of precursor into the plasma jet and in this study, a computational analysis for the heat and mass transfer around precursor droplets is presented that enables the estimation of zirconium acetate precipitation zones. Effects of droplet size, injection velocity and injection angle on droplet trajectory, droplet size reduction and surface temperature of axially injected droplets are investigated and the baseline cases are compared to the transversely injected droplets. It has been shown that the plasma temperature and velocity fields experienced by the axially injected droplets are significantly different than the transverse injection and the axially injected droplets heat-up much faster than the transversely injected droplets. The homogeneous nucleation hypothesis employed in this study suggests that the precipitation is observed at much earlier stages of the droplet lifetime for axial injection, when compared to the transverse injection. Further heat up of these droplets in the plasma is hypothesized to lead to the shattering of the formed crust and eventual break up of the internal liquid into droplets. Smaller droplets result in thicker shells and interconnected ceno-spherical structures. Very small droplets ($d \leqslant 5$ μm), result in full precipitation within the droplet and hence they are predicted to form solid spheres. Although there is experimental evidence suggesting shell-type structures are formed in transverse droplet injection into a plasma [24], experimental evidence is highly desirable to support these axial injection results.

Acknowledgements

The research presented here was financially supported by ONR Grant No. N000014-02-1-0171 under the direction of L. Kabacoff and S. Fishman. Authors would like to acknowledge Drs. N. Padture, E. Jordan and M. Gell for many fruitful discussions.

References

[1] A.G. Evans, D.R. Mumm, J.W. Hutchison, G.H. Meier, F.S. Pettit, Mechanisms controlling the durability of thermal barrier coatings, Prog. Mater. Sci. 45 (2001) 505–553.

[2] N.P. Padture, M. Gell, E.H. Jordan, Thermal barrier coatings for gas-turbine engine applications, Science 296 (2002) 280–284.

[3] Y. Wang, S. Jiang, M. Wang, S. Wang, T.D. Xiao, P.R. Strutt, Abrasive wear characteristics of plasma sprayed nanostructured alumina–titania coatings, Wear 237 (2000) 176–185.

[4] L. Pawlowski, P. Fauchais, Thermal transport properties of thermally sprayed coatings, Int. Mater. Rev. 37 (1992) 271–289.
[5] A. Kulkarni, J. Gutleber, S. Sampath, A. Goland, W.B. Lindquist, H. Herman, A.J. Allen, B. Dowd, Studies of the microstructure and properties of dense ceramic coatings produced by high-velocity oxygen-fuel combustion spraying, Mater. Sci. Eng. A369 (2004) 124–137.
[6] R.C. Tucker, Plasma and detonation gun deposition techniques and coating properties, in: R. Bunshah (Ed.), Deposition Technologies for Films and Coatings, Park Ridge, NJ, 1982, pp. 454–489.
[7] S.Y. Semenov, B.M. Cetegen, Experiments and modeling of the deposition of nanostructured alumina–titania coatings by detonation waves, Mater. Sci. Eng. A335 (2002) 67–81.
[8] B.M. Cetegen, S.Y. Semenov, D. Goberman, Deposition of multi-layered alumina–titania coatings by detonation waves, Scr. Mater. 48 (2003) 1483–1488.
[9] N.P. Padture, K.W. Schlichting, T. Bhatia, A. Ozturk, B.M. Cetegen, E.H. Jordan, M. Gell, S. Jiang, T.D. Xiao, P.R. Strutt, E. Garcia, P. Miranzo, M.I. Osendi, Towards durable thermal barrier coatings with novel microstructures deposited by solution-precursor plasma spray, Acta Mater. 49 (2001) 2251–2257.
[10] E.H. Jordan, L. Xie, X. Ma, M. Gell, N.P. Padture, B.M. Cetegen, A. Ozturk, J. Roth, T.D. Xiao, P.E.C. Bryant, Superior thermal barrier coatings using solution precursor plasma spray, J. Therm. Spray Technol. 13 (2004) 57–65.
[11] M. Gell, L. Xie, X. Ma, E.H. Jordan, N.P. Padture, Highly durable thermal barrier coatings made by the solution precursor plasma spray process, Surf. Coat. Technol. 177–178 (2004) 97–102.
[12] L. Xie, E.H. Jordan, N.P. Padture, M. Gell, Phase and microstructural stability of solution precursor plasma sprayed thermal barrier coatings, Mater. Sci. Eng. A381 (2004) 189–195.
[13] W. Yu, Diagnostics of the particle field in particle-laden dc-arc plasmas and high velocity combustion jets as applied to industrial therma sprays, Ph.D. thesis, University of Connecticut, 1999.
[14] B.M. Cetegen, W. Yu, In-situ particle temperature, velocity, and size measurements in dc arc plasma thermal sprays, J. Therm. Spray Technol. 8 (1999) 57–67.
[15] J. Karthikeyan, C.C. Berndt, J. Tikkanen, S. Reddy, H. Herman, Plasma spray synthesis of nanomaterial powders and deposits, Mater. Sci. Eng. A238 (1997) 275–286.
[16] A. Ozturk, B.M. Cetegen, Modeling of plasma assisted formation of precipitates in zirconium containing liquid precursor droplets, Mater. Sci. Eng. A384 (2004) 331–351.
[17] S.Y. Semenov, B.M. Cetegen, Spectroscopic temperature measurements in dc-arc plasma jets utilized in thermal spray processing of materials, J. Therm. Spray Technol. 10 (2001) 326–336.
[18] M.I. Boulos, P. Fauchais, E. Pfender, Thermal Plasmas, Plenum Press, 1994.
[19] M.C. Yuen, L.W. Chen, On drag of evaporating liquid droplets, Combust. Sci. Technol. 14 (1976) 147–154.
[20] B. Abramzon, W.A. Sirignano, Droplet vaporization model for spray combustion calculations, Int. J. Heat Mass Transfer 32 (1989) 1605–1617.
[21] A. Daif, M. Bouaziz, X. Chesneau, A. Ali-Cherif, Comparison of multicomponent fuel droplet vaporization experiments in forces convection with the Sirignano model, Exp. Therm Fluid Sci. 18 (1999) 282–290.
[22] G.L. Messing, S.C. Zhang, G.V. Jayanthi, Ceramic powder synthesis by spray pyrolysis, J. Am. Ceram. Soc. 76 (1993) 2707–2726.
[23] S.C. Zhang, G.L. Messing, Synthesis of spherical zirconia particles by spray pyrolysis, J. Am. Ceram. Soc. 73 (1990) 61–67.
[24] L. Xie, X. Ma, E.H. Jordan, N.P. Padture, T.D. Xiao, M. Gell, Identification of coating deposition mechanisms in the solution-precursor plasma-spray process using model spray experiments, Mater. Sci. Eng. A362 (2003) 204–212.
[25] G.V. Jayanthi, S.C. Zhang, G.L. Messing, Modeling of solid particle formation during solution aerosol thermolysis, Aerosol Sci. Technol. 19 (1993) 478–490.
[26] W.M. Kays, M.E. Crawford, Convection Heat and Mass Transfer, McGraw-Hill, New York, 1993.
[27] G.J. vanWylen, R.E. Sonntag, Fundamentals of Classical Thermodynamics, John Wiley & Sons, New York, 1986.